

## Stability of conducting fluid flow between coaxial cylinders under thermal gradient and axial magnetic Field

Hamza Benhacine<sup>1</sup>, Brahim Mahfoud<sup>2\*</sup>, Mohamed Salmi<sup>3</sup>

<sup>1</sup>Department of Mechanical, Faculty of Technology, University of Mohamed Boudiaf, M'sila, Algeria.

<sup>2</sup>Materials and Sustainable Development Laboratory (LMDD), University of AMO-Bouira, Algeria

<sup>3</sup>Department of Physics, Faculty of Technology, University of Mohamed Boudiaf, M'sila, Algeria.

<sup>1,3</sup>Laboratory of physics and chemistry of materials, University of M'sila, Algeria.

### ARTICLE INFO

Received: Aug. 28 2021;  
Received in revised form:  
07 Dec. 2021;  
Accepted: 21 Dec. 2021;  
Published online:  
06 Jan. 2022

#### Keywords:

Bifurcation  
Coaxial cylinders  
Fluid layers  
Magnetic field  
Vortex breakdown  
Stability

### ABSTRACT

Numerical simulations were performed to investigate the bifurcation in swirling flow between two coaxial vertical cylinders produced by the thermal gradient. The suppressed effects of an axial magnetic field on both vortex breakdown and fluid layers are analyzed. The governing Navier-Stokes, temperature, and potential equations are solved by using the finite-volume method. A conducting fluid is placed in the gap between two coaxial cylinders characterized by a small Prandtl number ( $Pr = 0.032$ ). Three annular gaps were  $R = 0.7, 0.8,$  and  $0.9$  compared in terms of flow stability, and heat transfer rates. The combination of aspect ratio  $\gamma=1.5$  and Reynolds number,  $Re=1500$  is the detailed case in this study. In the hydrodynamic case, vortex breakdown takes place near the inner cylinder due to the increased pumping action of the Ekman boundary layer. In addition, the competition between buoyancy and viscous forces develops a fluid layered structure. It is shown that the onset of the oscillatory instability set in by increasing Reynolds number to the critical value. The results show that with an intensified magnetic field, the vortex breakdown disappears, the number of fluid layers will be reduced and the onset of the oscillatory instability will be retarded. Stability diagrams corresponding to the limits of transition from the multiple fluid layers to the one fluid layer are obtained.

© Published at [www.ijtf.org](http://www.ijtf.org)

### 1. Introduction

The external magnetic field is used by the tokamak powerful to confine and control the hot plasma of fusion fuels in a ring-shaped container called a 'torus'. Many researchers

are interested in this technology due to its enhanced performance compared with other approaches. The magnetic field keeps the hot plasma away from the machine walls. Two sets of magnetic coils-toroidal and poloidal create a complex 3D field to hold and shape plasma in

\*Corresponding e-mail: mahfoud.mah@gmail.com (Brahim Mahfoud)

**Nomenclature**

$B$	magnitude of the external magnetic field, Tesla	<i>Greek symbols</i>	
$E$	electric charges	$\alpha$	thermal diffusivity of the fluid, m <sup>2</sup> /s
$F_L$	Lorentz force	$\beta$	thermal expansion coefficient, 1/K
$H$	height of the cylinder, m	$\gamma$	aspect ratio (H/R <sub>o</sub> )
$Ha$	Hartmann number	$\nu$	kinematic viscosity of the fluid, m <sup>2</sup> /s
$J$	dimensionless current density	$\mu_0$	magnetic permeability, H/ m
$Nu$	Nusselt number	$\mu_0$	polytropic exponent
$\overline{Nu}$	average Nusselt number	$\rho$	density of the fluid, kg/m <sup>3</sup>
$P$	dimensionless pressure	$\sigma$	electric conductivity, $\Omega$ /m
$Pr$	Prandtl number	$\Phi$	dimensionless electric potential
$R$	annular gap, m	$\Omega$	angular velocity, rad/s
$Re$	Reynolds number	$\Psi$	non-dimensional stream function
$R_o$	radius of the outer cylinder, m	$\Theta$	dimensionless temperature
$R_{in}$	radius of the inner cylinder, m	$\tau$	dimensionless time
$Ri$	Richardson number		
$V$	velocity vector		

the magnetic ‘cage’ The plasma is generated by sou blowing a small quantity of the fusion gazes (deuterium and tritium) into the container and breakdown it by using a high voltage to the neutral gas to form an electrically charged plasma, which can be controlled by the magnetic field.

A great plasma current is induced in the center as the primary of a transformer, which the plasma is the secondary winding. This current starts heating the plasma to fusion temperatures. Additional plasma heating is provided by neutral beam injection and microwave systems. Excess heat from the hot fusion plasma is exhausted using a magnetic ‘divertor’; streams of plasma are ‘diverted’ into special heat resistant plates at the top and bottom of the tokamak. The geometry of the coaxial shape plays an important role in the removal of excess heat. Many types of research are performed on this matter concerning different geometries, heat transfer, and magnetic fields. Several researchers, [1, 2] are investigated a geometry consisting of two coaxial cylinders in which a liquid metal was placed in the annular gap while a helium gas was flowing inside the inner cylinder. They showed that in such a design, the interior gas can upgrade the heat transfer. Similar configurations were used by Kakarantzas et al.

[3] and Mahfoud et al. [4] where a liquid metal is placed between two coaxial vertical cylinders. They showed that the damping of the magnetic field results in fluid deceleration and consequently flow stabilization.

Convection problems in the literature review confirmed that a magnetic field is used to stabilize the perturbation in the fluid motion and control the velocity field [5–11]. The influence of the geometry and the thermal gradient to generate small vortices with and without an applied magnetic field have been studied by [12–13]. In the hydrodynamic case, the increase of rotation rate accelerates the fluid and leads to the creation of a vortex breakdown bubble that occurred on the inner cylinder. The bottom disk in basic flow serves as a pump, drawing in fluid axially and driving it away in an outward spiral In closed coaxial cylinders, this fluid swirls along the annular gap and then spirals to the fixed top disk, then again turns into the axial direction towards the rotating bottom disk. The conservation of angular momentum causes an initial increase in swirl velocity, by the spiraling motion and so the creation of a concentrated vortex [11]. Effects of magnetic field on heat transfer using the nanofluid are also studied by many researchers [14, 15]. Some researchers have detailed the position and length of a vortex

under a magnetic field, as revealed in the studies of [16–17]. Laouari *et al.* [18] have recently studied the central position of the vortex and the limits of appearance and disappearance of the vortex breakdown in the different conductivity regimes. Then they have established stability diagrams corresponding to the transition from the vortex zone to the no-vortex zone for insulating and electrically conducting walls. Mahfoud *et al.* [19–20] investigate the behavior of vortex breakdown in vertical annuli under the axial magnetic field. The results obtained showed that the vortex breakdown is suppressed beyond the magnitude of the magnetic field exceeds a critical value and before the suppression of the electric vortex occurs.

In this paper, the first section presents forced convection without and with a magnetic field. The second section includes the mixed convection without and with magnetic effect. The first objective is to clarify the effects of the annular gaps on vortex breakdown (apparition, and suppression) in which three annular gaps are compared. The second objective is to identify the magnetic field intensity corresponding to eliminate the vortex bubble. The third objective is to clarify the temperature gradient role on the appearance of the bifurcation in form of fluid layers. Finally, the aim is to specify the magnetic field intensity corresponding to removing the fluid layers. Therefore, we present the stability limits correspond to the domain where the layering does not occur.

## 2. Flow configuration and model

A viscous conducting fluid characterized by a small Prandtl number ( $Pr = 0.032$ ) rotates in the annular gap ( $R$ ) between two coaxial vertical cylinders with height ( $H$ ). The combined stabilizing action of the external magnetic field and thermal gradient are imposed in the vertical direction which is schematically plotted in Fig. 1 Three annular gaps ( $R = 0.7, 0.8$  and  $0.9$ ) are examined. The case of aspect ratio,  $\gamma (H/R_o) = 1.5$  and Reynolds number,  $Re=1500$  are detailed. The annular gap is defined as ( $R = R_o - R_{in}$ ), where  $R_{in}$ ,  $R_o$  are the radius of the internal and outer cylinders, respectively and  $R_o = 1.0$  in all cases.

A temperature difference ( $\Delta T$ ) is axially imposed (the top disk is hotter than the bottom). The fluid and solid walls system are subjected to an external axial magnetic field,  $\mathbf{B}$  ( $B_o \mathbf{e}_z$ ),  $\mathbf{e}_z$  is the unit vector in the  $z$ -direction. The lower disk rotates about the  $z$ -axis at an angular velocity  $\Omega$ , which is supposed constant, while the upper disk is fixed. The magnetic Reynolds number  $Re_m = \mu_0 \sigma \Omega R_o^2 \ll 1$ , that measure the ratio of induction to magnetic diffusion. In the specific problem, we can neglect the magnetic field induction by comparing it with the  $B_o$ . Also, the only effective force that remains is the electromagnetic force of Lorentz.

For simplification of the problem, some assumptions are given: (i) three fluids considered here are incompressible and Newtonian; (ii) properties of fluids are constants and appraised at the reference temperature; except the density, which is treated according to Boussinesq's approximation, (iii) Joule heating, and viscous dissipation terms are neglected. Similarly, (iv) the container walls are electrically insulated, and (v) radiation heat transfer is often ignored in this calculation.

The magnetohydrodynamic equations are dimensionless by the following quantities: the lengths  $R_o$ , time  $1/\Omega$ , velocities  $\Omega R_o$ , pressure  $\rho (\Omega R_o)^2$ , temperature,  $\theta = (T - T_0)/\Delta T$  and electric potential,  $B_o \Omega R_o^2$ . Also, the simulation considered the flow steady and laminar. So, the dimensionless equations can be defined as:

$$\nabla \cdot \mathbf{V} = 0 \quad (1)$$

$$\frac{\partial \mathbf{V}}{\partial \tau} + (\mathbf{V} \cdot \nabla) \mathbf{V} = -\nabla P + \frac{1}{Re} \nabla^2 \mathbf{V} + Ri \theta \mathbf{e}_z + \frac{Ha^2}{Re} (\mathbf{V} \times \mathbf{B}) \times \mathbf{B} \quad (2)$$

$$\frac{\partial \theta}{\partial \tau} + (\mathbf{V} \cdot \nabla) \theta = \frac{1}{Re \cdot Pr} \nabla^2 \theta \quad (3)$$

The induced electric current is given by the interaction of convective flow with the magnetic field,  $\mathbf{J} = \sigma(\mathbf{E} + \mathbf{V} \times \mathbf{B})$  hence, the electric charges become  $\mathbf{E} = -\nabla \Phi$ . Where vector velocity  $\mathbf{V}$  ( $v_r, v_\theta, v_z$ ), have the components in the radial ( $v_r$ ), azimuthal ( $v_\theta$ ) and axial ( $v_z$ ) direction, respectively. The conservation of the induced electric current  $\nabla \cdot \mathbf{J} = 0$  gives the electric potential.

$$\nabla^2 \Phi = \nabla \cdot (V \times B) \quad (4)$$

P,  $\Theta$ , and  $\Phi$  are the dimensionless pressure, temperature, and electric potential, respectively. Non-dimensional parameters are Reynolds number ( $Re = \Omega R_0^2 / \nu$ ); the Hartmann number ( $Ha = B_0 R_0 \sqrt{\sigma / \rho \nu}$ ); the Richardson number ( $Ri = \beta g \Delta T / \Omega^2 R_0$ ). Two other non-dimensional parameters control the comportment of the flow: the aspect ratio ( $\gamma = H / R_0$ ) and the Prandtl number ( $Pr = \nu / \alpha$ ). The symbols  $\rho$ ,  $\nu$ ,  $\beta$ ,  $\alpha$ , and  $\sigma$  denote, respectively, the density, the kinematic viscosity, the thermal expansion, the thermal diffusivity, and electric conductivity. The Lorentz force is given by  $F_L = J \times B$ , which are in the  $r$ ,  $z$ , and  $\theta$  directions, respectively:

$$\begin{cases} F_{Lr} = -1/r \cdot \partial \Phi / \partial \theta - v_r \\ F_{Lz} = 0 \\ F_{L\theta} = \partial \Phi / \partial r - v_\theta \end{cases} \quad (5)$$

with the current density,  $J$  is:

$$\begin{cases} J_r = -\partial \Phi / \partial r + v_\theta \\ J_z = -\partial \Phi / \partial z \\ J_\theta = -1/r \cdot \partial \Phi / \partial \theta - v_r \end{cases} \quad (6)$$

All simulations were performed starting from  $\tau=0$ . The bottom disk starts its rotation with angular velocity  $\Omega$ , while the top and side walls are stationary, respectively. No-slip boundary conditions on solid walls are affected ( $v_r = v_\theta = v_z = 0$ ), and which are also electrically insulated ( $\partial \Phi / \partial n = 0$ ). The boundary conditions are  $v_\theta = r$  and  $\Theta = -1/2$  at a rotating cold bottom disk and  $v_\theta = 0$  and  $\Theta = 1/2$  at a stationary hot top disk. Owing to the geometrical symmetry, the periodicity conditions are  $V(r, \theta, z) = V(r, \theta + 2\pi, z)$ .

The stream function  $\Psi$ , which is specified as:

$$v_r = 1/r (\partial \Psi / \partial z), \quad v_z = -1/r (\partial \Psi / \partial r) \quad (7)$$

The heat transfer and convection mode are concluded from the average Nusselt number which is calculated at the bottom disk as:

$$\overline{Nu} = \left( \frac{1}{\pi} \right) \int_0^1 \int_0^{2\pi} Nu(r, \theta) r d\theta dr \quad (8)$$

$$\text{where } Nu(r, \theta) = \gamma \left( \frac{\partial \Theta}{\partial z} \right) \Big|_{z=0}$$

**Table 2**

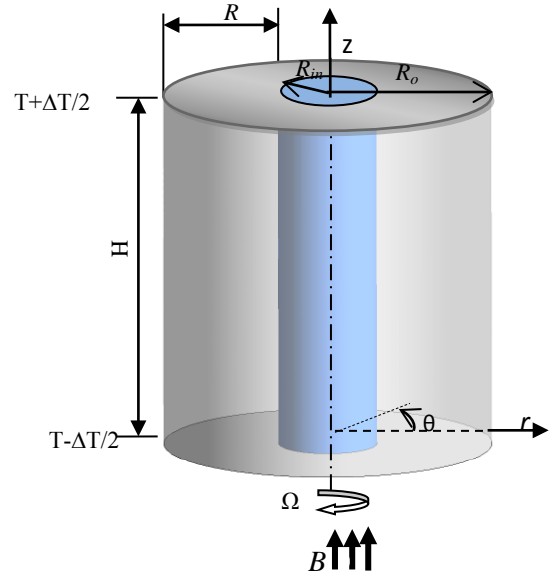


**Fig. 1.** Flow geometry

### 3. Numerical method and grid employed

The governing equations and boundary conditions of the system mentioned above are discretized by the finite volume method and solved by the tridiagonal matrix algorithm TDMA. SIMPLER scheme Patankar [21] was selected to solve the coupling between velocity and pressure. The central-difference approximation scheme is used for the diffusion and convective terms.

In this simulation, three staggered nonuniform meshes were applied to get better convergence and are listed in Table 1. The influence imposed by the thinner Hartmann layers ( $\sim 1/Ha$ ), and annular gap lead adoptngted this grid for precision and time-saving. The details of check grid dependence have been examined using as a parameter for comparison the average Nusselt number,  $\overline{Nu}$  (see Table 2).

**Table 1**

Grid sizes used in the numerical simulations

Annular gap	Grid( $r, \theta, z$ )
$R=0.7$	70x70x70 $\gamma$
$R=0.8$	80x80x80 $\gamma$
$R=0.9$	90x90x90 $\gamma$

Grid independence test for the case of  $Re=1500$  and  $\gamma=1.5$  when  $Ri=1.0$ , and  $Ha=5$ .

	$R=0.7$	$\overline{Nu}$	$R=0.8$	$\overline{Nu}$	$R=0.9$	$\overline{Nu}$
<b>Grid(<math>r,\theta,z</math>)</b>	60x60x90	0.6698	70x70x105	0.6703	80x80x120	0.6710
	70x70x105	0.6710	80x80x120	0.6722	90x90x135	0.6735
	80x80x120	0.6711	90x90x135	0.6722	100x100x150	0.6736

### 4. Results and Discussion

First, the used numerical model has been validated by comparing the present numerical results with the numerical results of Mahfoud et al. [9] and Kakarantzas et al. [3] who investigated the flow and heat transfer of liquid metal which rotates in the annular of concentric cylinders under a magnetic field effect. Fig. 2 shows the reproduction of the radial distribution of axial velocity in the middle of the domain, for  $Ha=100$  and the aspect ratio  $\gamma=2.0$  when the annular gap is  $R=0.4$  and the Rayleigh number  $Ra=10^5$ . Although, there is a good agreement between the compared numerical results.

The second comparison is tested against the numerical results of Yu, Li & Thess [16], as shown in Fig.3. It shows the effects of the magnetic field on the central position of the vortex on the z-axis for the case when the top disk is electrically conducting. In this case, the aspect ratio,  $\gamma=1.5$  when  $Ha=0$  and  $Ha=7$  at different Reynolds numbers, which is in the range of  $900 < Re < 1900$ .

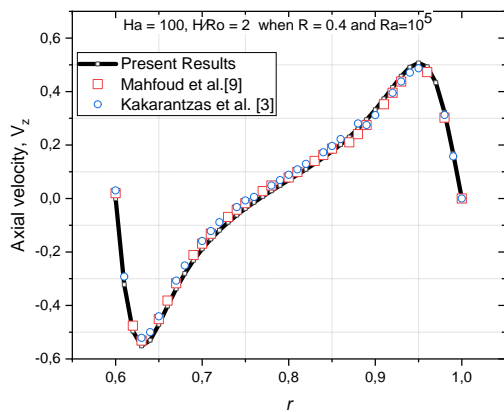


Fig. 2. Comparison with Mahfoud et al. [9] and Kakarantzas et al. [3].

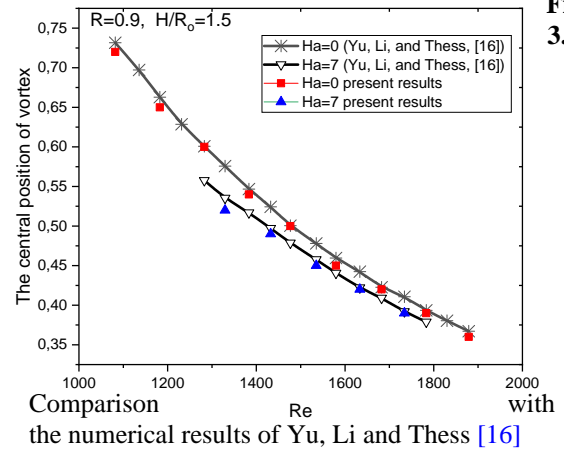
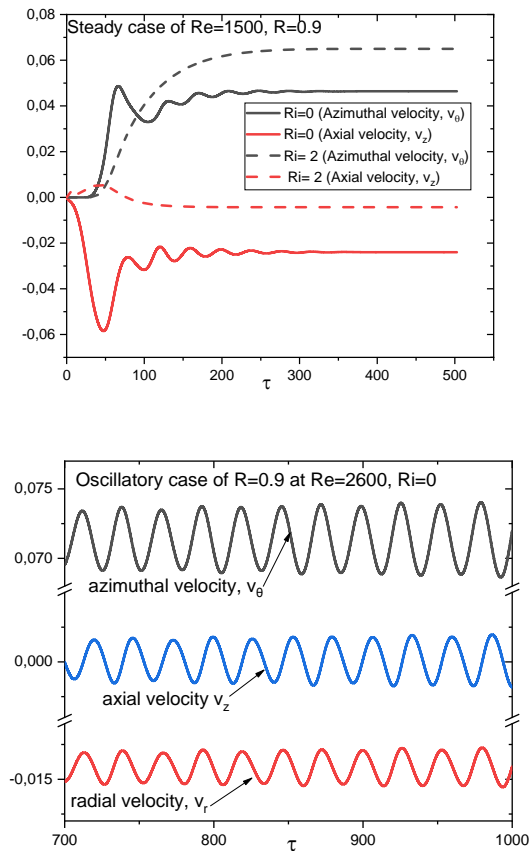


Fig. 3.

Results of numerical simulations are presented for one aspect ratio,  $\gamma=1.5$ , and three annular gaps ( $R=0.7, 0.8$ , and  $0.9$ ). An electrically conducting fluid is placed in the gap between two coaxial cylinders characterized by a small Prandtl number ( $Pr=0.032$ ) corresponding to the PbLi 17 alloy, which is in the most appropriate position to ensure the fusion blankets. The Richardson number analyzed here covers the range of  $0 \leq Ri \leq 2.0$ . Multiple magnetic intensities characterized by Hartmann numbers are used to suppress both vortex breakdown and fluid layers.

The problem considered could be oscillatory or turbulent; the following section includes the justification. It is known that the typical sequence of evolution of a dynamic system towards chaos for increasing values of the control parameter consists of the following stages: transition to an oscillatory or periodic state; a quasi-periodic regime, and finally chaos (or turbulence). To detect the regime of flow, i.e. transient or steady-state, a series of numerical calculations are performed for each case. Fig. 4 shows the temporal evolutions of axial and azimuthal velocities at the monitoring point ( $r=0.5, z=0.75$ ). These simulations presented steady-state solutions obtained for the various case  $Re=1500, R=0.9$

and the ranges of controlling parameters: the Richardson number ( $Ri = 0$  and  $Ri = 2.0$ ) and the Prandtl number ( $Pr = 0.032$ ), as shown in Fig. 4(upper). The oscillatory aspect of the temporal evolutions of the axial of axial radial and azimuthal velocities at the same monitoring point ( $r = 0.5, z = 0.75$ ) is shown in Fig. 4 (lower) for  $Re = 2760, Ri = 0$ . It is seen that the increase of  $Re$  enhances the fluid motion while the evolutions become time-dependent (oscillatory). Therefore, as the Reynolds number is increased, swirl strength increases, and hence the ability of waves to propagate against the flow increases [22]. The swirling flows will be steady and axisymmetric till the critical Reynolds numbers  $Re_{cr} \approx 2585$  when the oscillatory instability begins to set in for  $R = 0.9$  at  $\gamma = 1.5$ .



**Fig. 4.** Evolution of the velocities, at the monitoring point ( $r = 0.5, z = 0.75$ ).

#### 4.1 Annular gaps effect

The influence of the annular gaps on the flow pattern, the apparition, and suppression of vortex breakdown is also depicted in Fig. 5 where four Reynolds numbers ( $Re = 1500, 1750, 2000, 2250,$  and  $2500$ ) are compared for one aspect ratio  $\gamma = 1.5$  and three annular gaps  $R = 0.7, 0.8,$  and  $0.9$ , respectively. The first line of Fig. 5 shows the swirling flow in the cases of  $R = 0.7, 0.8$  and  $0.9$ , they are represented schematically by the streamlines in meridional planes for  $Re = 1500$ . When the annular gap is increased ( $R = 0.7, 0.8,$  and  $0.9$ ), the vortex appears at  $R = 0.9$  in which, the central position of the vortex on the  $z$ -axis is at  $z = 0.91$  and on the  $r$ -axis is  $0.19$ . The case of  $Re = 1750$  is shown in the second line of Fig. 5, in which a small vortex breakdown appears at  $0.8$ . Then the size of the vortex grows very quickly with the increasing annular gap to  $R = 0.9$ . The  $z$ -dimensionless length is  $0.17$  when  $R = 0.8$  and  $0.21$  for  $R = 0.9$ . The size of the breakdown grows with the increase of Reynolds number to  $Re = 2000$  in both cases ( $R = 0.8, 0.9$ ). As clearly shown by the streamlines on the case of  $Re = 2250$  that a small vortex appears at  $R = 0.7$ , on the other hand, the size of the vortex decreases for  $R = 0.9$  and remains the same for  $R = 0.8$ . As the Reynolds number,  $Re$  of case  $R = 0.7$  increases ( $Re = 2500$ ), the size of the vortex increases and vice versa. The behavior in the case of  $R = 0.9$  is the opposite because the vortex size decreases with the increase of  $Re$ .

For the hydrodynamic case, the diagram presented in Fig. 6 gives the stability limit in the  $(Re, \gamma)$  plane within which a vortex breakdown bubble occurred near to sidewall of the inner cylinder. The influence of the annular gaps on vortex breakdown zones in the  $(Re, \gamma)$  plane shows how the boundaries of the vortex breakdown shift. Three separate curves represent the limits of three-zone, i.e., the domains with and without vortex breakdowns could be observed. We observe that the decrease of the annular gap causes the decrease in the vortex breakdown zone so that the decrease in the values of the annular gaps causes boundaries to move towards the side of the lower aspect ratio.

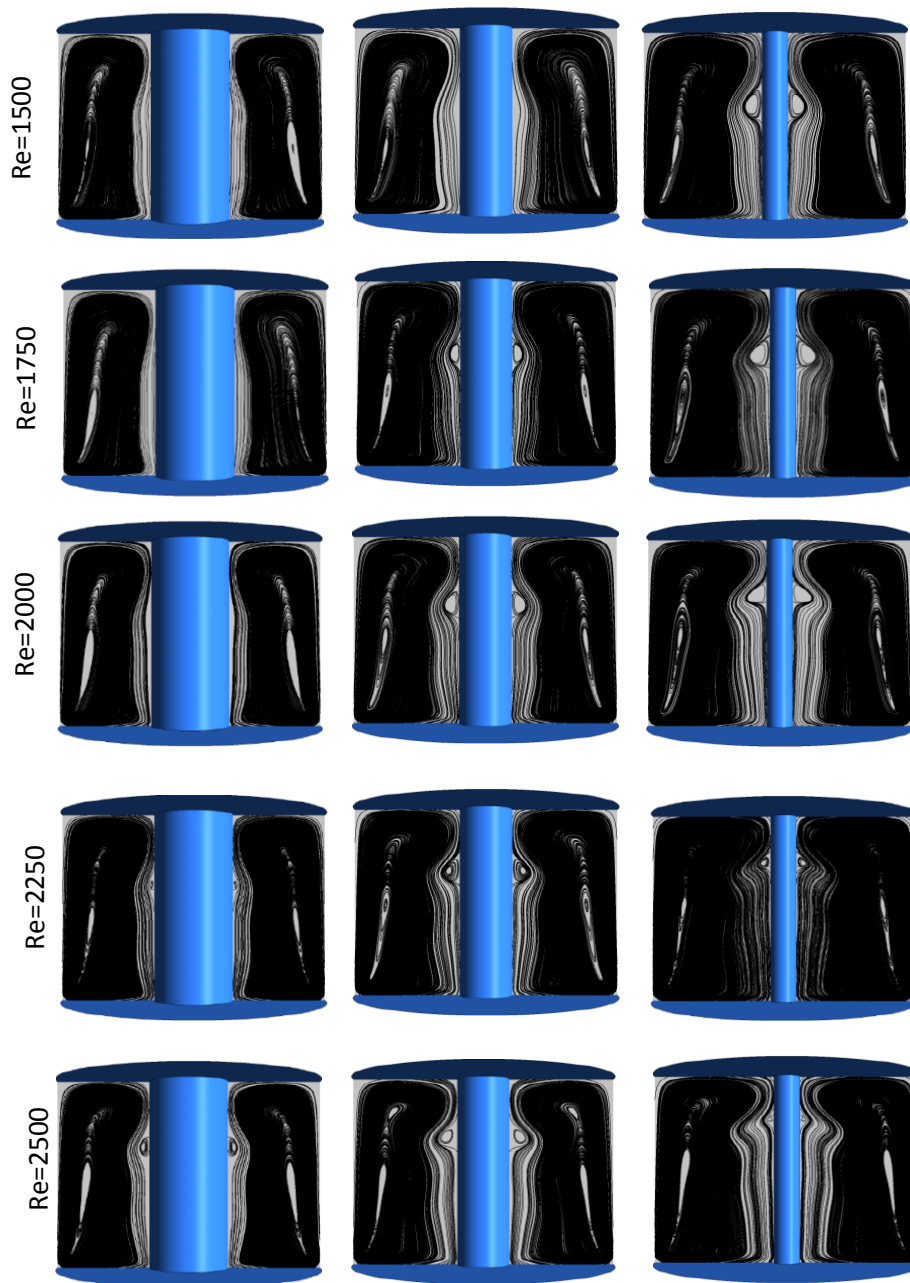


**Fig. 5.** Iso-contours of the stream function in case of  $\gamma=1.5$  for three annular gaps  $R=0.7, 0.8$  and  $0.9$  at different Reynolds numbers,  $Re$ .

#### 4.2 Magnetic field effects on vortex breakdown

This section clarifies the effects of the magnetic field to control the central position of the vortex on the  $z$ -axis and  $r$ -axis, respectively. The second stage is to identify the most

efficient  $Ha$  to eliminate the vortex bubble. The swirling flow in the annular gap produced by the rotating bottom disk under an axial magnetic can be divided into three regions, i.e., the core region, the Hartmann layer, and the side layer (Robert layer). The viscous forces can compete with magnetic forces in the Hartmann layer near to walls normal the

applied magnetic field.

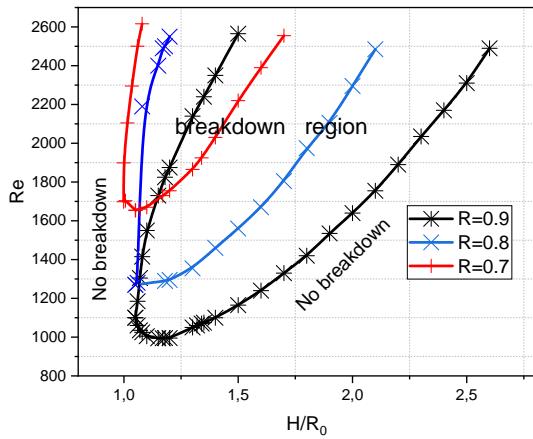


**Fig. 6.** Stability diagram in the  $(Re-\gamma)$  plane for annular gaps  $R=0.7, 0.8$  and  $0.9$ .

Thus, when the Hartmann number increases, the Ekman layer is progressively replaced by the Hartmann layer, which is near to walls normal to the magnetic field. These layers are perpendicular to the magnetic field, having a dimensionless thickness  $\delta_{\perp} \approx 1/Ha$ . Therefore, the intensified magnetic field results in Hartmann layer thickness. Where the walls are electrically insulating, the Hartmann layer near the disk has a similarity solution as in the case of the classical Ekman layer. The order of magnitude of the axial velocity is  $v_z \sim Re/Ha^3$  [18], which results in the weakness of the axial velocity. Pao and Long [23] also that an external magnetic field that intensifies magnetic intensity results in boundary layer thickness and a decrease of the axial flow component.

Fig. 7 shows streamlines for increasing Hartmann numbers ( $Ha=1, 5, 7$  and  $9$ ) in three case of  $Re = 1300$  (above),  $Re= 1500$  (middle), and  $Re= 2000$  (bellow) when  $R=0.9$  and  $\gamma=1.5$ . For  $Re= 1300$ , the vortex appears at  $Ha=1$  in which, the central position of the vortex on the  $z$ -axis is at  $z \approx 0.84$  and on the  $r$ -axis is  $0.15$ . Then the size of the vortex grows with the increasing  $Ha$  to  $5$ . The  $z$ -dimensionless length is  $0.18$  when  $Ha=1$  and  $0.11$  for  $Ha = 5$ , and disappears for critical Hartmann number ( $Ha_{cr} \approx 6.5$ ). The case of  $Re=1500$  is shown in the second line of Fig. 7, in which the vortex breakdown size diminishes

with increasing Hartmann numbers and finally disappears at  $Ha=9$ . For  $Re=2000$ , the vortex breakdown size rises with increasing Hartmann numbers and disappears for a value that exceeds  $Ha=9$ . Fig. 7 show that the size of the breakdown grows with increasing Reynolds number. So, the central positions of the vortex on the  $z$ -axis increase with increasing  $Re$  and  $Ha$ , respectively.

Fig. 8 (a, b) shows the effects of the magnetic field on the central position of the vortex on the  $z$ -axis and  $r$ -axis, respectively in the case of  $\gamma=1.5$  when the annular gap is  $R=0.9$ . Here, the central position is presented at different Reynolds numbers, which is in the range of  $1100 \leq Re \leq 2500$ . Without a magnetic field, a vortex appears at  $Re = 1170$  and disappears at  $Re = 2510$ . The central position on the  $z$ -axis is at  $z = 0.780$  when the small vortex appears at  $Re = 1175$  and rise to  $z = 1.157$  until  $Re = 2500$ . In Fig. 8a, the central positions of the vortex increase gradually with the increasing Hartmann number at a fixed Reynolds number. The effects of the magnetic field on the central positions of the vortex are much stronger for  $Ha=9$  since the vortex appears close to  $Re = 1690$  and disappears at  $Re = 2210$ . The central positions are at  $z= 1.029$  and  $1.14$  for  $Re = 1700$  and  $Re=2200$ , respectively. The results show that when the Hartmann number increase, the vortex breakdown is gradually suppressed by the magnetic field. In Fig. 8b, the central position of the vortex on the  $r$ -axis under an axial uniform magnetic field is different from those in the central position on the  $z$ -axis. In this case, the distribution of the central position on the  $r$ -axis represents the shape of a semicircle. As shown, their positions diminish gradually under the increasing effect of the magnetic field. When the Hartmann number increases, the central positions of the vortex on the  $r$ -axis drop at a fixed Reynolds number. Taking  $Re = 1800$  for example, the central positions of the vortex are at  $r = 0.201, 0.189, 0.179$  and  $0.139$  for  $Ha = 0, 5, 7$  and  $9$ , respectively.

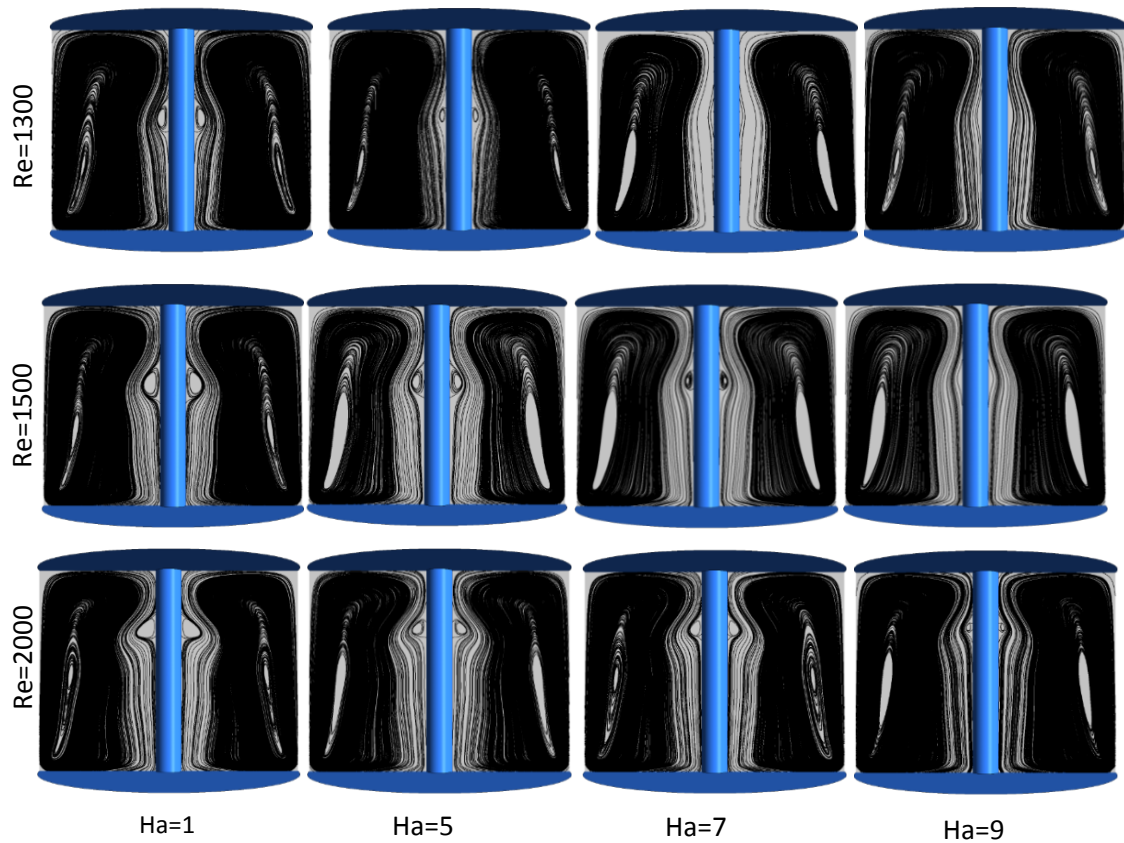


**Fig.7:** Streamlines in the meridional planes in three case of  $Re = 1300$  (above),  $Re = 1500$  (middle), and  $Re = 2000$  (bellow) when  $R=0.9$  and  $\gamma=1.5$  for progressively increasing Hartmann numbers ( $Ha = 1, 5, 7, 9$ )

At  $Ha=0, 5$ , and  $7$  the central positions on the  $r$ -axis are divided into two parts, when  $Re \leq 1800$ , the  $r$ -central position of vortex increase with the increasing  $Re$ , contrarily when  $Re \geq 1800$ , they decrease with the increasing  $Re$ . Finally, for the case of  $R=0.9$  at  $\gamma=1.5$ , the present results show that the increase of the  $Ha$  causes the increase of the  $z$ -central position of the vortex, but contrarily causes the decrease of the  $r$ -central position of the vortex breakdown. The situation can be interpreted as follows, the peak occurred in the region where the viscous and inertial forces are of the same magnitude. Moreover, Based upon experiments of Escudier [24], the breakdown region is characterised by a radius  $r$ , the corresponding Reynolds number is then  $(r/R_0)Re^{1/2}$ . The largest value of this quantity for

the case of  $R=0.9$  and  $\gamma=1.5$  at  $Ha=0$  is for  $Re=1800$  when  $r/R_0 \sim 0.202$  and  $(r/R_0)Re^{1/2} \sim 8.57$ . Fig. 8c shows the relationships between Reynolds number of base flow and Reynolds number of breakdown region. The rotation rate of the breakdown region increase up to  $(r/R_0)Re^{1/2} \sim 8.57, 8.02, 7.59, 5.93$  for  $Ha = 0, 5, 7$  and  $9$ , respectively and drops slowly when the Reynolds number is increased. In Fig. 8d, the dimensionless lengths of the vortex for the case of  $R=0.9$  at  $\gamma=1.5$  are presented when the Reynolds number is in the range of  $1100$  to  $2500$  with the increment of  $100$ . In  $Ha \neq 0$ , the magnetic field gives a stronger influence on the length especially to the peak value, and this exhibition is more obvious than that in  $Ha=0$ . When  $Ha = 5$  and  $Ha = 7$ , the lengths are  $\approx 0,19$  and  $0,15$  at the peak, respectively. For  $Ha = 7$ , the vortex appears close to  $Re = 1650$ , reaches the peak,

0.1014, at  $Re = 1700$  and disappears at  $Re = 2300$ .

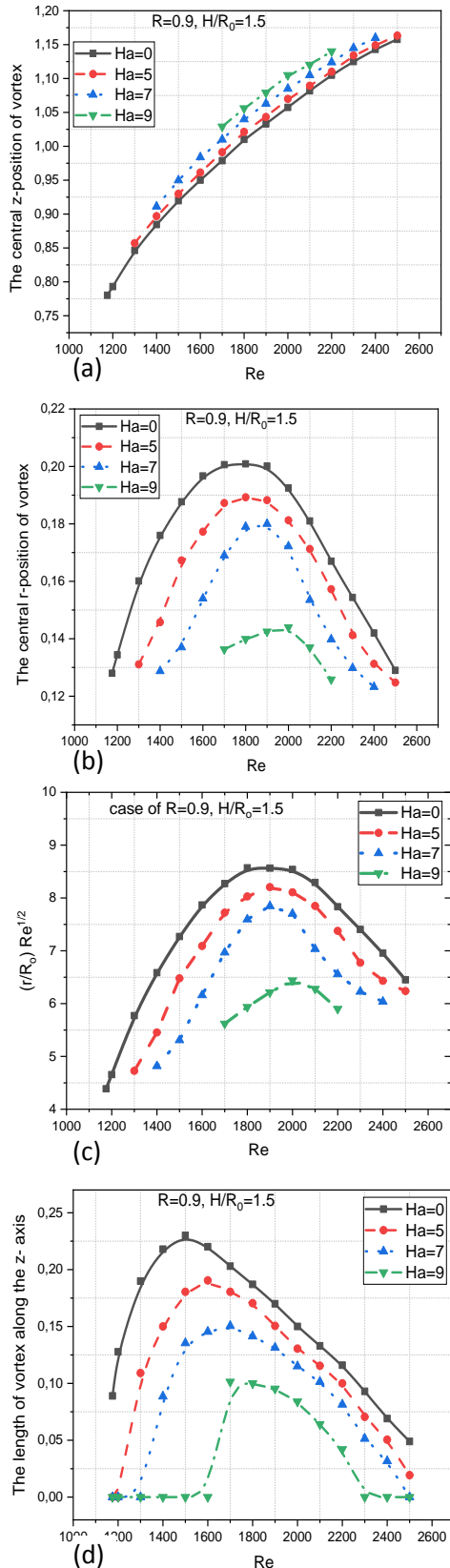


**Fig. 8.** The central position and the length of the vortex on the z-axis vs  $Re$

Stability limits for  $Ha=0$  and 5 at the annular gap  $R=0.9$  are constructed on  $(Re, \gamma)$  plane for two cases as shown in Fig. 9. There, curves represent the boundaries for the vortex zone and no-vortex zone and the limits between steady and unsteady zones. The boundaries shift shows that intensifying magnetic intensity contract the domain limits of the vortex breakdown. To obtain the impact of the Hartmann number on vortex breakdown zones, two selected magnitudes of Hartmann number,  $Ha=0$  and 5 have been studied. The black curve with start symbols shows the boundaries vortex breakdown at  $Ha = 0$ . For  $Ha = 5$ , the vortex breakdown zone boundaries shown by the curve in red colour with circle symbols shrink and shift upward concerning the  $Ha=0$  curve. Hence, this makes the increasing effects of the Hartmann number reduces the limits within which a vortex breakdown occurs and raises the transition to an unsteady regime [25].

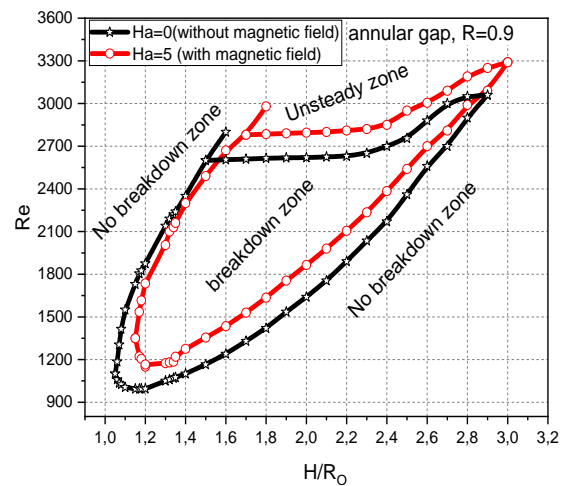


**Fig. 9.** Stability diagram in the  $(Re-\gamma)$  plane for  $Ha=0$  and 8 at the annular gap  $R=0.9$ .

### 4.3 Buoyancy effect on vortex breakdown and the fluid layers

To investigate the effects of thermal gradients on the fluid layers and the control of the vortex breakdown (i.e. location, or suppression of vortex breakdown), three annular gaps are compared ( $R=0.7, 0.8$ , and

0.9), which correspond to  $Re = 1500$  and  $\gamma = 1.5$  fields, in which forced convection takes place. Fig. 10. The case ( $Ri = 0$ ) corresponds to a decoupling of the velocity and temperature

fields, in which forced convection takes place.

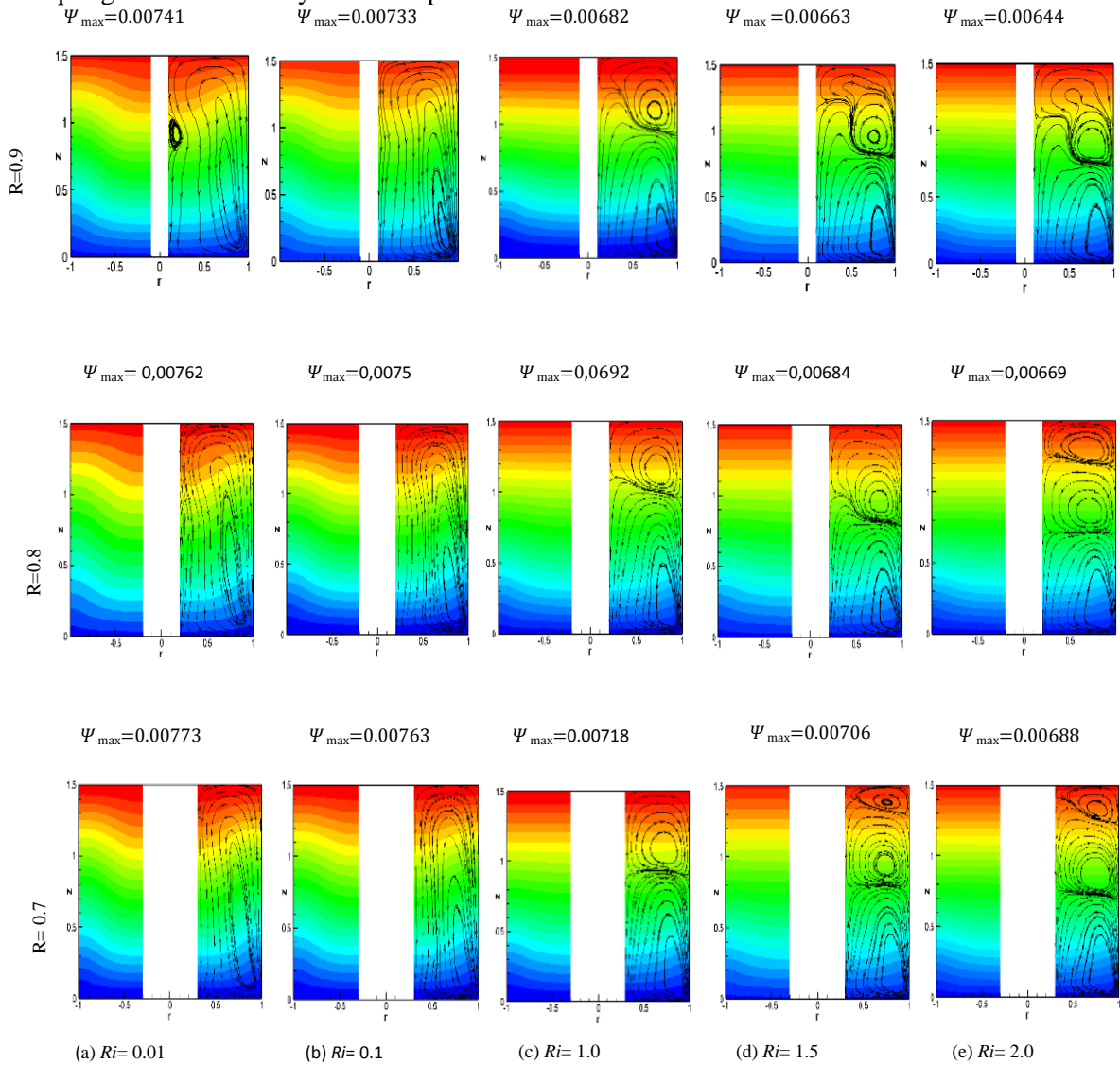


**Fig. 10.** Superposed streamlines and isotherms in meridional planes for progressively increasing Richardson numbers when  $Re=1500$ ,  $\gamma=1.5$  and  $Pr=0.032$ .

The rotation of the bottom gives a centrifugal force to the fluid, and this force drives the fluid radially outward. As the fluid stopped by the outer cylinder sidewall it is turned upward, producing jets. The upward jets and downward flow result in the centrifugal flow structure, with an axial vortex near the inner cylinder axis. This behavior incurs a

breakdown, with a single bubble. Fig. 10 presents the superposed streamlines and isotherms in meridional planes for progressively increasing Richardson numbers. The results for  $R=0.9$  show that when the Richardson number,  $Ri = 0.01$  the vortex breakdown remains effective. So, by increasing to  $Ri = 0.1$ , the vortex breakdown is suppressed. In this case, heat transfer convection is dominant. The maximum value

of the stream function decrease with increasing  $Ri$  until 0.0064 at  $Ri = 2.0$ . The streamlines when  $Ri = 1.0$  show a new region of counter-flow which grows with increasing  $Ri$  and then dominate the entire top section of the annular gap (plot first line of Fig. 10).

The plots in Fig. 10 for case  $R=0.8$  show the decomposition in the counter-flow region, up to two-layered appear for  $Ri = 1.0$ . The stratified structure with two fluid layers is observed when  $Ri = 2.0$ . Note that, the separated zone is curved and the top layer grows with increasing Richardson. The isotherms plot when  $Ri = 2.0$  shows that conduction mode dominated the heat transfer, especially in the top region. Similarly, the buoyancy acts for case  $R=0.7$  are stronger than those in cases  $R=0.9$  and  $R=0.8$  (plots in third line Fig. 10). When the vertical temperature gradient is small ( $Ri=0.1$ ), and the convection mode dominates heat flux, the vortex breakdown in the annular gap does not exist. In the range of  $Ri \geq 1$ , there is no big difference in the isothermal line distribution, but the maximum value of non-dimensional streamlines ( $\Psi_{max}$ ) decreases as the increasing of Richardson number, and are 0.00763 and 0.00688 at  $Ri=0.1$  and  $Ri=2$ , respectively, that indicates the flow is suppressed by the Buoyancy force. The process of increasing the Richardson number to  $Ri=1.0$  induces two stratified layers. On the range of  $Ri$  considered, up to three-layered appear for  $Ri = 1.5$  and  $Ri=2.0$  (Fig. 10d-e).

Fig. 11a shows the evolution of the number of fluid layers for the case of  $Re=1500$  and for  $R=0.7$ ,  $R=0.8$ , and  $R=0.9$  cases, which are discussed above. The number of layers is the number of stratified recirculation zones in the meridional flow. For  $R=0.9$ , the flow is characterized by one concentrated vortex when  $Ri = 0.01$ , this vortex undergoes breakdown, i.e. a stagnation point followed by a small recirculation zone near the inner cylinder wall. The flow contains a single layer, that occurs for  $Ri \leq 0.7$ . It was found also that the number of layers, corresponding to  $R=0.9$ , grows with the increase of Richardson number and leads to a second layer to form beyond  $Ri \geq 0.8$ . As to case  $R=0.8$ , a second layer flow structure is

observed when  $Ri \geq 0.6$ . In case  $R=0.7$ , up to three layers appear for  $Ri \geq 1.2$ .

Fig. 11b compares the maximum hydrodynamic streamlines ( $\Psi$ ) for the three annular gaps ( $R=0.7$ ,  $R=0.8$ , and  $R=0.9$ , respectively) when  $Re=1500$  and  $\gamma=1.5$ . The decreasing of the maximum value of hydrodynamic streamlines ( $\Psi$ ) with increasing  $Ri$  for all three cases proves that the intensified buoyancy affects the number of recirculation zones formed by swirling flow.

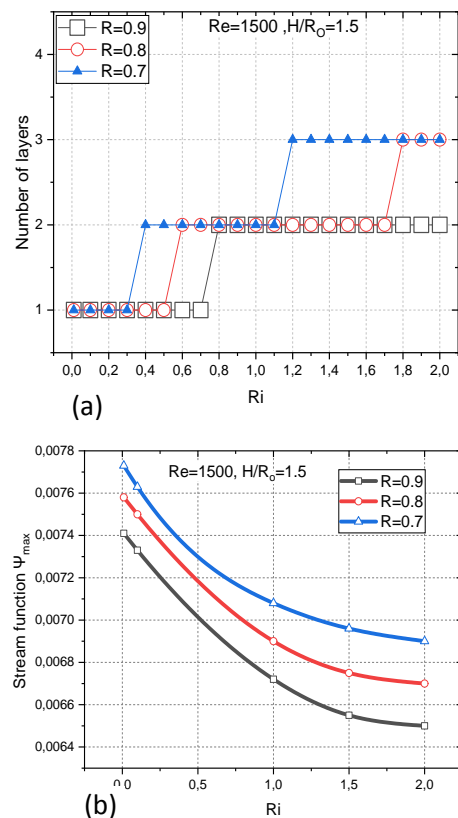


Fig. 11. Effect of Richardson number on the number of flow layers formed and on  $\Psi_{max}$ .

#### 4.4 Heat transfer

In this section, the relationship between the stratification of fluid and heat transfer will be clarified. However, the Nusselt number is analyzed in the remainder of this section for many parameters. The decreasing of the average Nusselt number with the Richardson number is presented in Fig. 12, where three

cases  $R=0.7$ ,  $R=0.8$ , and  $R=0.9$  are compared for  $Re=1500$  and  $\gamma=1.5$ . Fig. 12 shows that  $\overline{Nu}$  Monotonically decreases with increasing  $Ri$  and approaches the reciprocal of the aspect ratio, i.e.,  $1/H$  ( $=0.66$  at  $\gamma=1.5$ ) which means the value of the conduction limit.

In Fig. 12, it is noticed that the maximum value of  $\overline{Nu}$  is attained when a single layer fluid is established. For mixed convection, the influence of buoyancy force becomes stronger with the rising of the Richardson number, so the concurrence between viscous and buoyancy forces is increasingly important with increasing  $Ri$ . However, the lighter hot fluid close to the top hot disk sits on the top of the heavier cold fluid close to the bottom cold disk. The effects of natural convection continue to exist only near the heated top disk. In this case, the stable stratification of fluid opposes the flow produced by the bottom rotating disk, and so the net advective transport diminishes, and the value of  $\overline{Nu}$  decreases with increasing  $Ri$ . Also, these fluid layers play the role of thermal insulation, since the number of layers influences the heat transfer. We conclude that the combination of Richardson number and annular gaps control the heat transfer by the presence or absence of fluid layering. Furthermore, it is seen that at a constant value of  $Ri$  the average Nusselt values become progressively grow as the annular gap is increased indicating that advective transport reinforces with increasing  $R$ , as observed from Fig. 12. Consequently annular gap,  $R$  has an important influence on  $\overline{Nu}$  in this case.

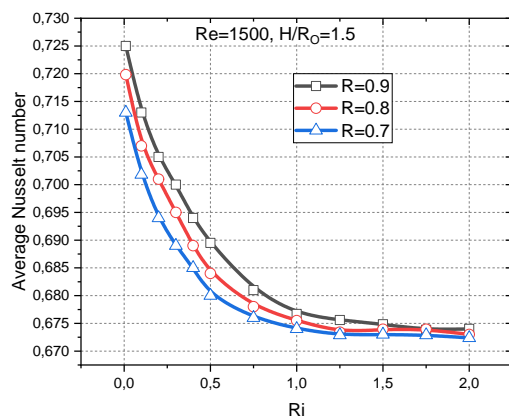


Fig. 12. Effect of the Richardson number on the

average Nusselt number.

#### 4.5 Magnetic effect on fluid layers

To investigate the effects of the axial magnetic field on the layering (i.e., apparition or suppression), taking, for example, the case of  $Re=1500$ ,  $\gamma=1.5$  and  $Ri=2.0$  at three cases mentioned above (i.e. case  $R=0.7$ ,  $R=0.8$ , and  $R=0.9$ ). The hydrodynamic streamline plots in the case of  $R=0.9$  at  $Ha=0$  show a double layer, in which the bottom layer is the biggest Fig. 13. The magnetic field in the vertical direction has a good suppressive effect on both vortex breakdown and fluid layers in which are shown in this case. As clearly shown by the streamlines on the first line of Fig. 13, the clockwise recirculation top region diminishes in size and moves toward the sidewall when  $Ha=10$ . On the contrary, the counterclockwise recirculation zone grows in size until it takes the entire top gap of the cylinder. Also, the maximum streamfunction decreases with increasing  $Ha$  and is 0.0064 and 0.0061 for  $Ha=0$  and  $Ha=10$ , respectively. The small toroidal vortex decreases in size and then disappears at  $Ha_{cr}=20$ . The r-central position of the small toroidal region rises with increasing  $Ha$  and, on the contrary, the z-central diminishes slightly. The central positions are at  $z=1.08$ ,  $0.99$ , and  $0.97$  for  $Ha=5$ ,  $10$  and  $15$ , respectively.

As for case  $R=0.8$  shown in Fig. 13, the streamline plots for  $Ha=0$ , show three layers, in which the top layer becomes narrow. The streamlines for  $Ha=5$  clearly show the two small toroidal vortices attached to the inner and outer wall, respectively. Another counterclockwise recirculation zone centered at  $z=0.82$  for  $Ha=5$  and decreases in size further and disappears at  $Ha=22$ .

The effect of increasing  $Ha$  is distinctly seen in Fig. 13 at case  $R=0.7$ . For  $Ha=0$  and  $Ha=5$ , three layers are observed, but at  $Ha=10$  the middle clockwise toroidal vortex divides into two cells and drives to the creation of two layers and stagnation-point [24] flow near to the inner wall. For  $Ha=20$  the streamlines show a small toroidal vortex centered at  $z=0.75$ , then decreases in size and disappears at  $Ha_{cr}=25$ . For all cases the isotherms plots when  $Ri$

=1.0 show that conduction dominate the heat transfer, especially in the top gap.

Fig. 14 compares the magnetic field effect on the number of fluid layers for three cases ( $R=0.7$ ,  $R=0.8$ , and  $R=0.9$ ) when  $Re=1500$  and  $Ri=2.0$ . The decrease in the curves as shown in Fig. 14 indicates that increasing  $Ha$  has an

important influence on the number of fluid layers formed. Therefore, the number of fluid layers decreases with increasing  $Ha$  for all three cases. For  $Ha=0$  we have three layers for case  $R=0.7$ , three layers for  $R=0.8$ , and two layers for  $R=0.9$ .

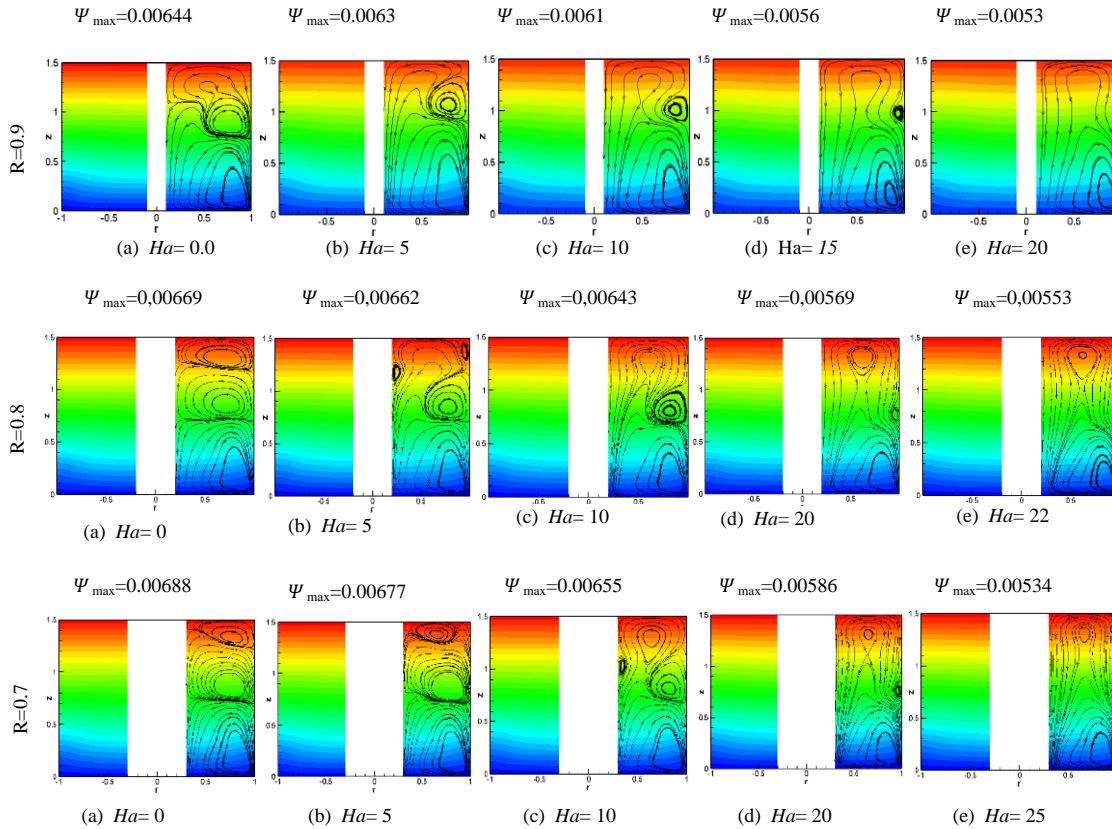


Fig. 13. Magnetic effect on streamlines and isotherms in meridional planes when  $Re=1500$ ,  $\gamma=1.5$  and  $Ri=2$

For  $Ha=10$  and  $15$ , two layers is observed for  $R=0.8$  and  $R=0.7$ , respectively. The critical Hartmann numbers,  $Ha_{cr} = 20, 22,$  and  $25$  correspondings to a single layer for cases  $R=0.7, 0.8$  and  $0.9$ , respectively. Consequently, the intensified magnetic reduces the number of resulting layers.

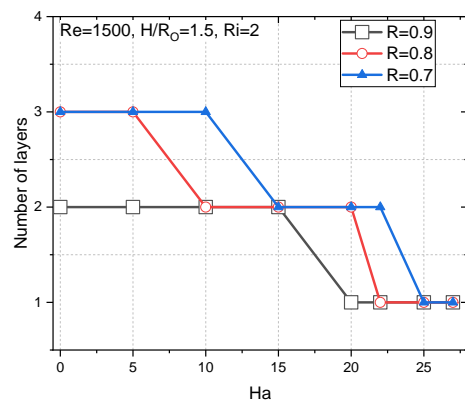
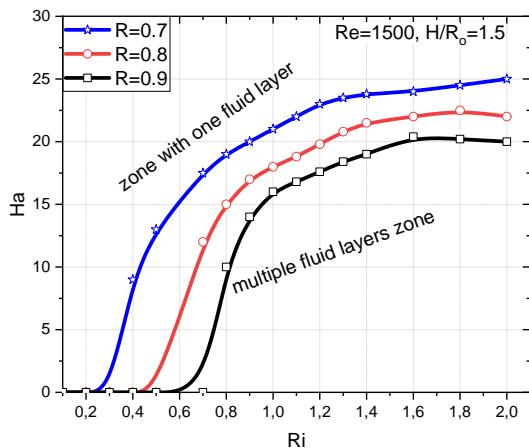


Fig. 14. Reduction of the number of fluid layers VS

Ha when  $Ri=2$  and  $Pr=0.032$ .

The diagram in the  $(Ha_{cr}-Ri)$  plane for all three cases when  $Re=1500$  and  $\gamma=1.5$  presented in Fig. 15 gives the evolution of critical Hartmann number  $Ha_{cr}$  versus  $Ri$ . There are three separate curves, represent the limits of two-zone, i.e., the domains with and without stratification fluid layers. The blue curve with star symbols in Fig. 15 represents the boundaries for the case of an annular gap,  $R=0.7$ . The red curve with a circle corresponding to case  $R=0.8$ . For case  $R=0.9$ , the threshold of transition is plotted by the black curve with square symbols. In all cases, we have seen that the increase of the  $Ri$  causes the increase of the  $Ha_{cr}$ . Also, increasing  $Ha$  removes the fluid layers at a constant value of  $Ri$  (the layering disappears after the amplitude of  $Ha$  goes beyond a critical value). The critical values ( $Ha_{cr}$ ) for case  $R=0.7$  are greater than those obtained in cases 0.8 and 0.9 for a fixed Richardson number.



**Fig. 15.** Diagram  $(Ha_{cr} - Ri)$  shows the limits of the transition from the multiple fluid layers zone to the single-layer zone.

## 5. Conclusion

Bifurcation and stability of mixed convection flow in the gap between two coaxial cylinders with a magnetic field have been numerically analyzed. The finite volume method has been used to capture the different vortex breakdowns in the isothermal case and the stratified layers under the temperature stratification condition. Three annular gaps

were compared in terms of flow stability, and heat transfer rates for one Prandtl number,  $Pr=0.032$ . One configuration of Reynolds number and aspect ratio are detailed. The main results obtained are as follows:

- It was shown that the domain in which a vortex breakdown bubble occurred decreases with decreasing annular gaps, so that the decrease in the values of the annular gaps, causes boundaries to move towards the side of the lower aspect ratio.
- The present results show that the increase of the Hartmann number shrinks the vortex breakdown zone
- In  $R=0.9$ , increasing Richardson number to 0.1 resulted in the suppression of vortex breakdown in which one layer occupied the annular gap.
- The stratification layers increase with increasing  $Ri$  for both cases  $R=0.8$  and  $0.9$ , but for the case,  $R=0.7$  more layers are developed.
- The fluid layers developed act to insulate the hot annular gap, so the average Nusselt number decrease with the increasing of stratified fluid layers.
- The number of stratified fluid layers increase with decreasing annular gap,  $R$
- The intensified magnetic field results lead to a decrease in the number of fluid layers
- Finally, the transition from multiple fluid layers to one fluid layer evolves with increasing  $Ri$ .

## References

- [1] F. C. Li, T. Kunugi, and A. Serizawa, MHD effect on flow structures and heat transfer characteristics of liquid metal–gas annular flow in a vertical pipe, *Int. J. Heat Mass Transfer* 48 (2005) 2571–2581.
- [2] A. Serizawa, T. Ida, O. Takahashi, and I. Michiyoshi, MHD effect of nak-nitrogen two phase flow and heat transfer in a vertical round tube, *Int. J. Multiphase Flow* 16 (1990) 761–788.
- [3] S. C. Kakarantzas, L. Benos, I. Sarris, B. Knaepen, A. Grecos, and N. Vlachos, MHD liquid metal flow and heat transfer between vertical coaxial cylinders under horizontal magnetic field, *Int. J. Heat and Fluid Flow* 65(2017) 342–351.
- [4] B. Mahfoud, A. Laouari, A. Hadjadj, H. Benhacine, Counter-rotating flow in coaxial cylinders under an axial magnetic field,

- European Journal of Mechanics-B/Fluids 78 (2019) 139–46.
- [5] B. Mahfoud, R. Bessaïh, Oscillatory swirling flows in a cylindrical enclosure with co-/counter-rotating end disks submitted to a vertical temperature gradient, *Fluid Dynamics & Materials Processing* 8 (2012) 1–26.
- [6] B. Mahfoud, R. Bessaïh, Stability of swirling flows with heat transfer in a cylindrical enclosure with co-/counter-rotating end disks under an axial magnetic field, *Numer. Heat Transfer, Part A* 61 (2012) 463–482.
- [7] B. Mahfoud, R. Bessaïh, Magnetohydrodynamic counter-rotating flow in a cylindrical cavity, *Int. J. Heat Mass Transfer* 93 (2016) 175–185.
- [8] B. Mahfoud, A. Bendjagholi, R. Bessaïh, Magneto-hydrodynamic co-rotating flow in a vertical cylindrical container, *Numer. Heat Transfer, Part A* 69 (2016) 1051–1063.
- [9] B. Mahfoud, H. Benhacine, A. Laouari, A. Bendjaghlouli, Magnetohydrodynamic effect on flow structures between coaxial cylinders heated from below, *J. Thermophysics and Heat Transfer* 34 (2020) 265–274.
- [10] J. K. Singh, G.S.Seth, P. Rohidas, Impacts of time varying wall temperature and concentration on MHD free convective flow of a rotating fluid due to moving free-stream with hall and ion-slip currents, *International Journal of Thermofluid Science and Technology*, 6, (2019), No. 19060301
- [11] M. Venkateswarlu, P. Bhaskar, Entropy Generation and Bejan Number Analysis of MHD Casson Fluid Flow in a Micro-Channel with Navier Slip and Convective Boundary Conditions, *International Journal of Thermofluid Science and Technology* 7, (2020), No. 070403
- [12] A. Bendjaghlouli, B. Mahfoud, D.E. Ameziani, Magnetohydrodynamic flow in a truncated conical enclosure, *Journal of Thermal Engineering* 5 (2019) 77–83.
- [13] A. Bendjaghlouli, D. E. Ameziani, B. Mahfoud, L. Bouragbi, Magnetohydrodynamic counter rotating flow and heat transfer in a truncated conical container, *J. Thermophysics and Heat Transfer* 33 (2019) 865–74.
- [14] S. Molli, K. Naikoti, MHD Natural Convective Flow of Cu-Water Nanofluid over a Past Infinite Vertical Plate with the Presence of Time Dependent Boundary Condition, *International Journal of Thermofluid Science and Technology*, 7 (2020), No. 070404.
- [15] B. Mahfoud, A. Bendjaghlouli, Natural convection of a nanofluid in a conical container, *Journal of Thermal Engineering*, 4(1) (2018) 1713–1723.
- [16] Y. Yu, B-W. Li, A. Thess, The effect of a uniform magnetic field on vortex breakdown in a cylinder with rotating upper lid, *Computers & Fluids* 88 (2013) 510–523.
- [17] SC. Dash, N. Singh, Influence of axial magnetic field on swirling flow and vortex breakdown zones in a cylindrical cavity with a rotating lid, *International Journal of Applied Mechanics* 11 (2019) 1950054.
- [18] A. Laouari, B. Mahfoud, and R. Bessaïh, A. Hadjadj, Hydrodynamic instabilities in swirling flow under axial magnetic field, *European Journal of Mechanics-B/Fluids* 85 (2021) 245–260.
- [19] B. Mahfoud, Magnetohydrodynamic effect on vortex breakdown zones in coaxial cylinders, *European Journal of Mechanics-B/Fluids* 89 (2021), 445–457
- [20] B. Mahfoud, Effects of an Axial Magnetic Field on Vortex Breakdown and Fluid Layer. *J. Appl. Fluid Mech.* 14 (2021) pp. 1741-1753,
- [21] S. Patankar, *Numerical Heat Transfer and Fluid Flow*, McGraw-Hill, New-York, 1980.
- [22] T. B. Benjamin, Theory of Vortex Breakdown Phenomeno, *J. Fluid Mech.* 14 (1962) 593–629.
- [23] HP. Pao, RR. Long, Magnetohydrodynamic jet-vortex in a viscous conducting fluid, *Quart J Mech Appl Math* 19 (1966) 1–26.
- [24] M. Escudier, Observations of the flow produced in a cylindrical container by a rotating endwall, *Experiments in Fluids* 2 (1984) 189–96.
- [25] H. Benhacine, B. Mahfoud, M., Salmi Stability effect of an axial magnetic field on fluid flow bifurcation between coaxial cylinders. *International Journal of Computational Materials Science and Engineering.* (2021) 2150023.